International Forum on Aeroelasticity and Structural Dynamics
IFASD 2019
9-13 June 2019, Savannah, Georgia, USA

FLUID-MODE FLUTTER IN PLANE TRANSONIC FLOWS

Jens Nitzsche[1], Lisa M. Ringel[1], Christoph Kaiser[1], Holger Hennings[1]

[1]Institute of Aeroelasticity, German Aerospace Center (DLR)
37073 Göttingen, Germany
jens.nitzsche@dlr.de

Keywords: Unsteady aerodynamics, transonic buffet, fluid-mode flutter, flow separation, aerodynamic resonance, p-k method

Abstract: We investigate the flutter behavior of 1) a typical-section OAT15A airfoil with a heave and a pitch degree of freedom and 2) a generic symmetric airfoil of variable thickness equipped with a flexible trailing-edge plate by means of RANS simulations. The linearized flutter stability problem in the pre-buffet region is approached with three different techniques: A Newton-based root search involving the p-k approximation (NPK), a rational function approximation (RFA) of the fluid-structure coupled frequency response and a time-domain eigenvalue identification on the coupled impulse response obtained via succesive convolution (SCM). We emphasize on flutter instabilities resulting from the coupling of a structural mode and a fluid mode in separated flow. We conclude that the buffet onset should be regarded as the flutter boundary in the limiting case of zero density and buffeting is essentially flutter.

1 INTRODUCTION

The natural growth of high-performance computing capacities has sparked an increasing interest in the routine solution of the Reynolds-averaged Navier-Stokes (RANS) equations to treat common aeroelastic loads and stability problems on industrial scale. That includes separated flow conditions far away from day-to-day aircraft operation [1]. A spectacular example of high-speed flow separation effects are large-scale, self-sustained recompression shock oscillations on the lifting surfaces, the so called transonic buffet or *shock buffet* phenomenon. It is known as a special case of a more general *aerodynamic resonance* behavior inherent to flows involving shock-induced separation, therefore being termed *pre-buffet flows* [2, 3, 4].

In the last decade a large portion of the scientific work on the matter has been devoted to the identification of the *shock buffet onset*, i.e. the critical parameter combination, at which the pre-buffet flow undergoes a Hopf bifurcation from a stable steady state to a stable unsteady limit-cycle solution. This search (for instance carried out by means of an eigenvalue-based global stability analysis of the RANS flux Jacobian [5, 6, 7, 8]) is motivated by the assumption that exceeding the buffet onset will result in large-scale airload fluctuations that eventually cause a detrimental elastic wing *response*, usually termed *buffeting*. In other words, the buffet onset as obtained for a non-moving fluid boundary marks the limit of safe operation. This excludes the possibility that an elastic reaction of the fluid boundary may have, in turn, an impact on the fluid eigenbehavior.

In comparison to full-grown shock buffet the motion-induced unsteady aerodynamics in the (pre-buffet) separated flow region and the impact on the flutter behavior has gained not much

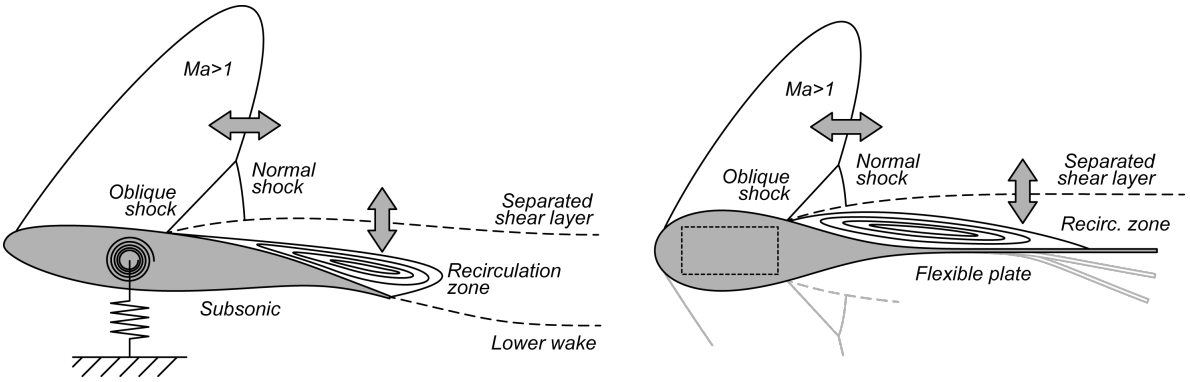

Figure 1: Schematic view of the two generic configurations investigated in this study: An elastically suspended 2-DOF OAT15A airfoil (left) and a symmetric flexible-plate airfoil (right).

interest so far. Instead, it is a rather common notion that due to the usually small values of the quasi-steady aerodynamic derivatives (e.g. $\partial c_L/\partial\alpha$) separated flows are much less inclined to induce flutter or critical unsteady airloads in general. In contrast, in [2] it was already shown that the emerging of an aerodynamic resonance peak while approaching the buffet onset involves the risk of one-degree-of-freedom flutter in the sense of negative aerodynamic damping for certain types of motion and in critical frequency ranges.

In this paper we investigate the flutter behavior of two plane airfoil configurations in transonic separated pre-buffet flow. In the first case and based on the availability of experimental and numerical reference data we choose the OAT15A airfoil [9, 10, 11, 12, 13] in combination with a generic heave-pitch structural dynamic model. In the second case we investigate a generic symmetric airfoil parameterization equipped with a variable-length flexible trailing-edge plate (**Figure 1**). As will be shown in this paper, the standard method for the solution of the linearized flutter stability problem, the p-k method, may miss flutter instabilities that result from the coupling of fluid modes and structural modes. We therefore investigate three alternative techniques, two working in the frequency domain and one being based entirely in the discrete time domain.

2 NUMERICAL MODELS AND METHODS

In this paper we aim at studying the effect of separated transonic flows at various steady operating points defined by Mach number and geometric parameters (e.g. angle of attack, airfoil thickness) on the flutter behavior of simple generic structures with well-defined properties. Aerodynamic model and structural model exchange information via generalized (modal) coordinates and generalized aerodynamic forces (GAF). The building blocks of the modelling approach, aerodynamic model, structural model and flutter analysis are described in the following.

2.1 Aerodynamic model

We use DLR's unstructured-mesh RANS solver TAU to compute the generalized aerodynamic forces. Spatial and temporal discretization is based on experience and follows a trade between accuracy and economic considerations. **Figure 2** and **Figure 3** show the two-dimensional RANS meshes used in this study. In the outer (separated) boundary layer and wake region an isotropic cell spacing of $\Delta x \approx 0.5\%$ is realized, while the wall-tangent and wall-normal cell stretching nowhere exceeds a value of 1.2. The farfield boundary is located 100 chord lengths

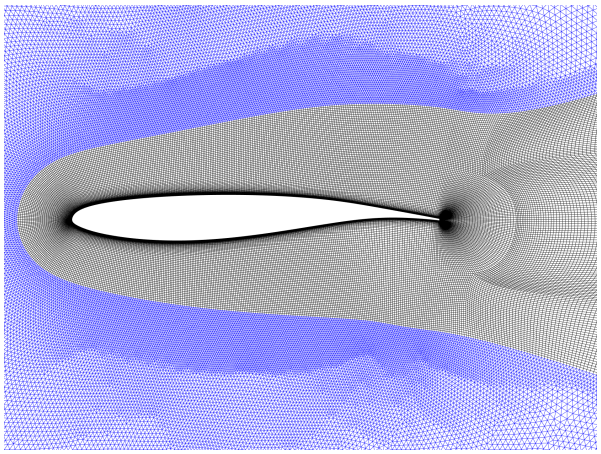

Figure 2: 2-d RANS mesh of the OAT15A airfoil ($\Delta x \approx 0.5\%$)

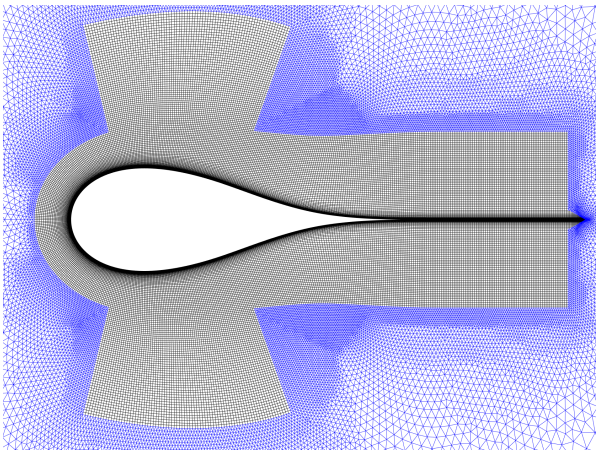

Figure 3: 2-d RANS mesh of parametric flex-plate airfoil ($t = 0.28, L = 0.4, \Delta x \approx 0.5\%$)

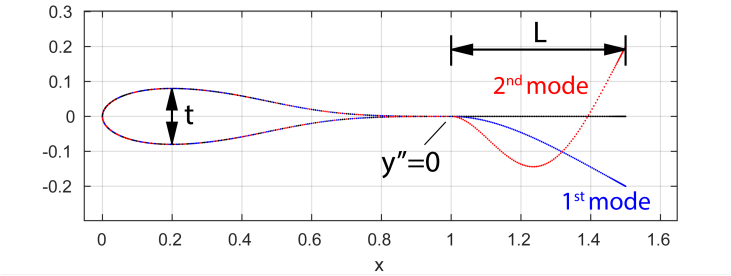

Figure 4: Parametric geometry of the symmetric flexible-plate airfoil

away from the airfoil to minimize the impact of numerical farfield reflections. The number of grid points amounts to 150-200 thousand. The meshes are convergent with respect to steady integral lift, drag and moment values. We employ a central Jameson-style scheme with matrix dissipation in space and an implicit BDF2 scheme in time. The non-dimensional simulation time step size $\Delta t^* = \Delta t \cdot V/c$ is fixed at 2.5%. As the baseline turbulence model, mainly for reasons of robustness, we use the Spalart-Allmaras (SA) model. Other models are occasionally employed to investigate the turbulence modelling influence. To propagate the mode shapes as prescribed on the airfoil surface to the surrounding volume mesh radial-basis function interpolation is used.

The symmetric flex-plate airfoil is defined through a generic C^2-smooth parametric curve including the maximum thickness t and the plate length L as the main parameters (**Figure 4**). The curve reaches a chosen thickness and curvature at $x_t = 0.2$. At the trailing edge $x = 1$ the airfoil curve returns to zero thickness, zero slope and zero curvature. The trailing plate has zero thickness, starts at $x = 1$ and can have arbitrary length. The reference chord length, nevertheless, keeps the value of $c = 1$ m.

In the case of the OAT15A airfoil two types of grid motion are applied: A rigid-body heaving motion orthogonal to the free-stream velocity vector and a rigid-body pitching motion around quarter-chord point. The GAF response to a pitching rotation around an arbitrary rotation center along the chord can be synthesized via weighted superposition of the heave response and the original quarter-chord pitch response without any noticeable error. In the case of the flex-plate airfoil two types of motion are imposed on the the surface consisting of the first and second

bending mode shape of an homogeneous Euler-Bernoulli cantilever beam with length L and starting at the trailing edge $x = 1$.

During an unsteady simulation run the airfoil surface is deflected with a *small-amplitude* unit impulse at one single time step only and the response of the GAFs (being the scalar projection of the field of aerodynamic forces on the surface onto the elastic mode shape) is recorded and stored for later use in the flutter calculations. A "zero run" without any motion is recorded as well and subtracted later to guarantee a return of the net impulse response to exact zero for time towards infinity.

For the OAT15A airfoil, the Reynolds number is fixed at $Re_A = 3$ million and for the parametric flex-plate airfoil is fixed at $Re_A = 1$ million (independent of the plate length L).

2.2 Structural model

The structural equation of motion

$$M\ddot{q} + D\dot{q} + Kq = Q \tag{1}$$

with the generalized coordinates q and the generalized external forces Q follows in the 2-d OAT15A airfoil case the classical typical-section form:

$$\begin{bmatrix} m & S_\alpha \\ S_\alpha & I_\alpha \end{bmatrix} \begin{pmatrix} \ddot{h} \\ \ddot{\alpha} \end{pmatrix} + \begin{bmatrix} D_h & 0 \\ 0 & D_\alpha \end{bmatrix} \begin{pmatrix} \dot{h} \\ \dot{\alpha} \end{pmatrix} + \begin{bmatrix} K_h & 0 \\ 0 & K_\alpha \end{bmatrix} \begin{pmatrix} h \\ \alpha \end{pmatrix} = \begin{pmatrix} -L \\ M \end{pmatrix} \tag{2}$$

with

$$m = \mu_{ref}\rho_{ref}\pi c^2/4 \quad S_\alpha = x_\alpha cm \quad I_\alpha = r_\alpha^2 c^2 m \quad K_h = \omega_h^2 m \quad K_\alpha = \omega_\alpha^2 I_\alpha$$
$$\omega_h = \omega_{h,ref}^* V_{ref}/c \quad \omega_\alpha = \omega_{\alpha,ref}^* V_{ref}/c$$

Having a wind tunnel experiment in mind we assume that the center of gravity could ideally be placed at a pitching axis location of 40% chord. This would lead to a decoupled mass matrix. We calibrate the structural stiffness to meet an arbitrarily chosen reduced frequency combination at a reference Mach number of $Ma_{ref} = 0.73$. Since we assume constant temperature ($T = 273.15$ K), the free-stream velocity, and hence, the reduced structural vacuum eigenfrequencies are a function of Mach number. The rather high mass ratio μ is based on the assumption of extra tuning weights to balance the c.g. location. A high mass ratio is also favorable to avoid premature static divergence. The baseline structural configuration is defined as

$$c = 1\ \mathrm{m} \quad \rho_{ref} = 1.225\ \mathrm{kg\ m^{-3}} \quad V_{ref} = 241.84\ \mathrm{m\ s^{-1}}$$
$$\mu_{ref} = 50 \quad x_\alpha = 0 \quad r_\alpha^2 = 0.1 \quad \omega_{h,ref}^* = 0.1 \quad \omega_{\alpha,ref}^* = 0.2$$

Occasionally, we vary the structural eigenfrequencies of the system to $(\omega_{h,ref}^* = 0.2, \omega_{\alpha,ref}^* = 0.3)$ and $(\omega_{h,ref}^* = 0.3, \omega_{\alpha,ref}^* = 0.4)$ to study the effect of stiffness.

In the case of the flat plate attached to the parametric airfoil we assume an Euler-Bernoulli cantilever beam of length L, clamped at $x = 1$. Mass and stiffness matrix are diagonal. If the analytical mode shapes (see Figure 4) are scaled to a maximum deflection of 2, the modal mass matrix diagonal entries become

$$m_i = L\rho_p h_p$$

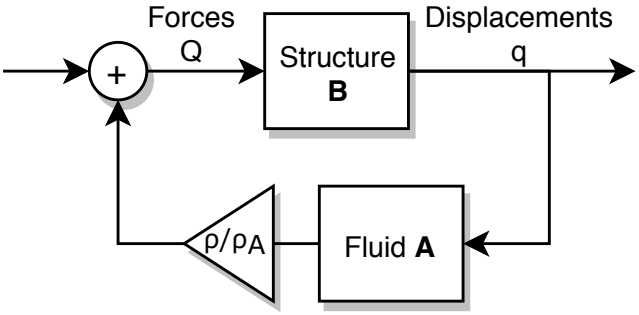

Figure 5: Aeroelastic feed-back loop with the system parameter ρ

The eigenfrequencies read as

$$\omega_i = \gamma_i^2 \frac{h_p}{L^2} \sqrt{\frac{E}{12\rho_p}} \quad \text{with } \gamma_i = \{1.875, 4.694\}$$

and the stiffness matrix diagonal entries become $k_i = \omega_i^2 m_i$. Example values for steel are $E = 210$ GPa and $\rho_p = 7850$ kg m^{-3}. The plate height h_p can be scaled to meet a certain frequency requirement.

2.3 Flutter analysis

For the flutter stability investigations we assume the scenario of a (de-)pressurized wind tunnel. At constant Mach number, temperature and free-stream velocity we virtually increase the air density ρ (**Figure 5**). Since we keep the velocity constant while increasing density the *reduced* vacuum eigenfrequencies of the structure stay constant as well. Note that the flutter analysis is a pure post-processing step following the computationally expensive production of the aerodynamic impulse responses which are, for economic reasons, sampled at a single pair of density ρ_A and Reynolds number Re_A only. Thus, the virtual density sweeps to study the aeroelastic system eigenvalues will match the CFD conditions at one selected point only. The repercussions of this common *non-matched* flutter analysis approach are beyond the scope of this study.

We compare three different methods to obtain the aeroelastic eigenvalues as a function of ρ, two frequency domain methods and one time domain method.

2.3.1 Frequency domain

The transfer function of the aeroelastic system in **Figure 5** reads as

$$H = (1 - \frac{\rho}{\rho_A} AB)^{-1} B \tag{3}$$

and translates with

$$B(s) = \left(s^2 M + sC + K\right)^{-1} \tag{4}$$

to

$$H(s, \rho) = \left[s^2 M + sC + K - \frac{\rho}{\rho_A} A(s)\right]^{-1} \tag{5}$$

with s denoting the Laplace variable. To obtain the complex poles we follow two alternative strategies from here:

1. Direct Newton-based root search for the complex pairs (λ , x) that solve the nonlinear eigenvalue problem
$$\left[\lambda^2 M + \lambda C + K - \frac{\rho}{\rho_A} A(\lambda)\right] x = 0$$
with the well-known disadvantage that samples of $A(s)$ are usually available only along the imaginary axis and hence A(s) must be approximated throughout the complex plane, most commonly via $A(s = \Im(s)i)$, known as the "p-k" concept and therefore here referred to as Newton-p-k (NPK).

2. Exact evaluation of Equation 5 at $s = i\omega$ to construct the frequency response function (FRF) of the coupled system first. Subsequently, a rational function is fitted (RFA) to the FRF data. The main disadvantage here is that a choice for the order of the denominator polynomial RFA is needed as an input, that leads the way to over-/under-fitting including the production of non-physical poles. The RFA itsself is obtained by the Vector Fitting method [14].

Since the NPK method is by nature very sensitive to the initial values of the Newton iteration, a good estimator for the starting values is needed. The most obvious choices are the vacuum eigensolutions when starting at zero density and continue from there in the following. Additionally, we enrich the starting values with the RFA approximations and random values.

For both methods NPK and RFA the tabulated aerodynamic FRF input data is the result of a discrete Fourier transform of the time-domain CFD unit impulse responses: $A_{ij}(i\omega) = \mathcal{F}\{a_{ij}(t)\}$. The FRF production fails if the aerodynamic impulse response itself is unstable, i.e. the aerodynamic response amplitude is growing instead of decaying like in the self-excited shock buffet case. The SCM technique, to be described in the following, does not suffer from this fundamental drawback.

2.4 Time domain

We employ an experimental successive convolution method (SCM) to directly synthesize the coupled impulse response sequence h from the known aerodynamic impulse response a (already weighted with ρ/ρ_A) and the analytically derived structural dynamic impulse response b. The coupled impulse response at time i can be derived as

$$h_i = (1 - c_0)^{-1} \left(a_i + \sum_{k=0}^{i-1} c_{i-k} h_k \right) \tag{6}$$

with $c = a * b$ denoting the open-loop impulse response sequence. In the first step, at impulse time zero, h is initialized with $h_0 = (1-c_0)^{-1} a_0$. Note that for the specific case of fluid-structure coupling the structural dynamic impulse response b always starts at zero and thus $b_0 = 0$ and $c_0 = 0$.

Due to the purely algebraic nature of the SCM algorithm the synthesized coupled solution is *exact*. No additional coupling error as known from staggered nonlinear CSM-CFD solution schemes is introduced. In a certain sense Equation 6 is the discrete-time counterpart of Equation 3. In the case of multiple degrees of freedom the formalism stays intact, except that a, b and h are matrix-valued.

Once the coupled impulse response sequence h is available we employ the Ibrahim time-domain (ITD) algorithm [15] to recover the eigenvalue and eigenvector information buried in the discrete time signals. This surprisingly powerful identification method is also at the core of the Dynamic Mode Decomposition (DMD) method, that recently gained some attention in the experimental and computational fluid dynamics community and has recently been applied in the shock buffet context [16]. The key idea of the method is in the first place to least-square fit a linear operator G that maps a set of solution vectors W_i stored in the snapshot matrix X_i (also known as block Hankel matrix) to their immediate successors X_{i+1}:

$$X_{i+1} = GX_i \tag{7}$$

with

$$X_i = \begin{bmatrix} W_i & W_{i+1} & \dots & W_{i+n} \\ W_{i+1} & W_{i+2} & \dots & W_{i+n+1} \\ \vdots & \vdots & \ddots & \vdots \\ W_{i+m} & W_{i+m+1} & \dots & W_{i+m+n} \end{bmatrix} \tag{8}$$

The over-determined system Equation 7 can be solved with standard methods. The eigenvalues μ_i of G are transformed to the continuous-time equivalent λ_i via

$$\lambda_i = \frac{\log \mu_i}{\Delta t} \tag{9}$$

with Δt denoting the time step size. If the size of W_i is large (e.g. CFD field solutions) a data compression pre-processing step via Proper Orthogonal Decomposition (POD) may be necessary, that also facilitates the solution of Equation 7. The ITD/DMD method yields physical and non-physical poles. The latter need to be eliminated by a pole selection strategy during which the sought physical complex eigenvalues should stabilize with increasing block size m (and possibly POD truncation size). The resulting eigenvalues λ_i and eigenvectors $\tilde{W}_i$ approximate the input snapshot sequence by

$$W(t) = \sum_i \alpha_i \tilde{W}_i e^{\lambda_i t} \tag{10}$$

which is the expected general behavior of linear time-invariant (LTI) systems. The application of the method to the output time series of *dynamically nonlinear* systems will lead to non-predictable and likely non-physical results and should therefore be avoided. An exception to this are stable limit-cycle solutions (LCO). In this case ITD/DMD will necessarily yield the fundamental frequency of the LCO plus the corresponding nonlinear higher harmonics. All real parts of λ_i, however, will be zero in this case as the amplitudes stay constant over time.

3 RESULTS

3.1 OAT15A airfoil typical section

In the beginning, we choose a global quasi-steady perspective on the investigated aerodynamic parameter space. **Figure 6** shows the results of 45×41 steady solutions with the SA turbulence model processed with regard to the streamwise location of the upper-side recompression shock (pressure gradient maximum). At moderate transonic Mach numbers three distinct regions can be observed: Subsonic (no shock detectable at all), regular shock motion (shock moves downstream with increasing angle of attack) and so called *inverse* shock motion (shock moves upstream with increasing AoA. The latter is a reliable indicator for shock-induced flow

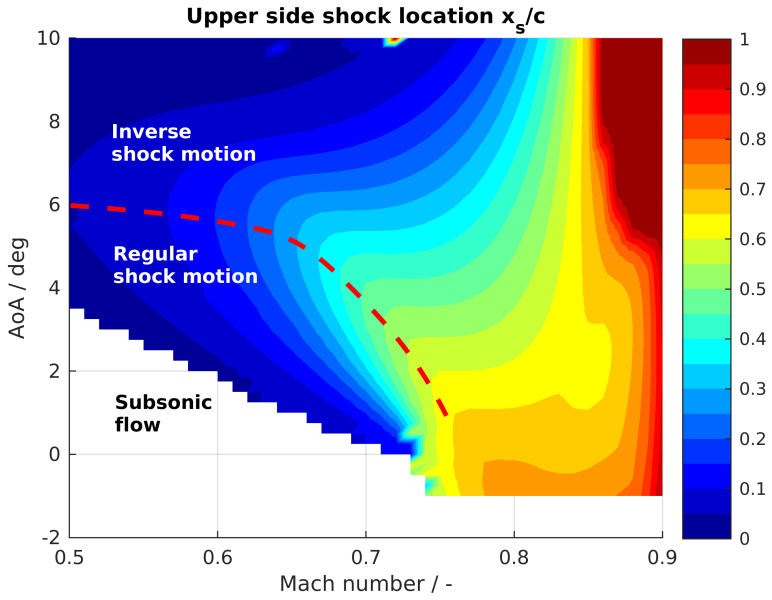

Figure 6: The quasi-steady lift polar slope $\partial c_L/\partial\alpha$ of the OAT15A airfoil as a function of Mach number and angle of attack.

separation or, in other words, over-proportional boundary layer thickening downstream of the shock. Inverse shock motion serves well as a necessary condition for the occurrence of unsteady aerodynamic resonance as the shock oscillation itself usually exhibits a near-$180°$ phase drop from inverse to regular shock motion at the resonance frequency [2]. **Figure 7** shows the lift polar and the shock location at the prominent Mach number of $Ma = 0.73$, that has been investigated in a previous wind tunnel experiment [10]. Specifically, we study the effect of turbulence modelling. Rather large deviations can be noted in the maximum-lift region. All of the four eddy viscosity models (SA, SST, Wilcox, LEA) predict stable steady solutions. Only the Reynolds-stress model (RSM) solutions are unstable in a AoA range $4.5° \leq \alpha \leq 6.75°$ and degenerate into full-grown shock buffet, an observation similar to [11].

To estimate the shape of the expected Transonic Dip flutter boundary, we inspect the quasi-steady lift curve slopes $\partial c_L/\partial\alpha$ at different Mach numbers and angles of attack and compare

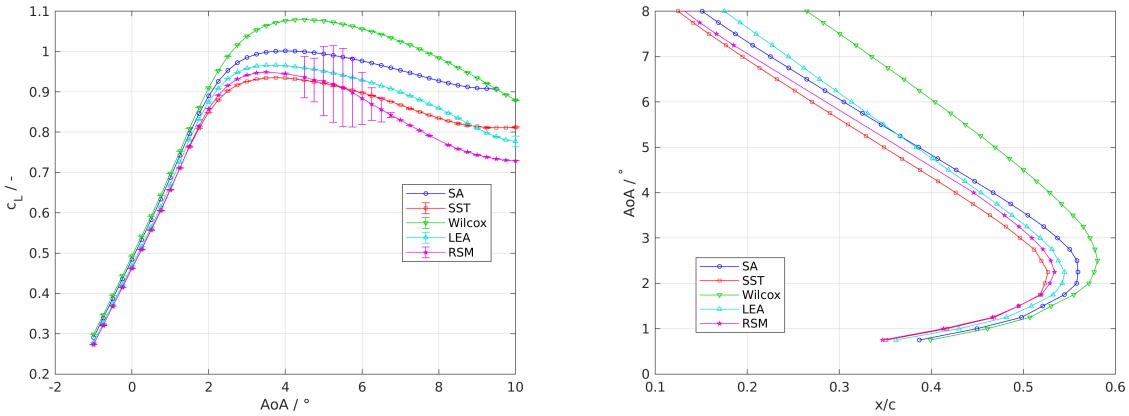

Figure 7: The effect of turbulence modelling on the steady OAT15A solutions at $Ma = 0.73$: Lift c_L (left) and upper-side shock position as a function of angle of attack α

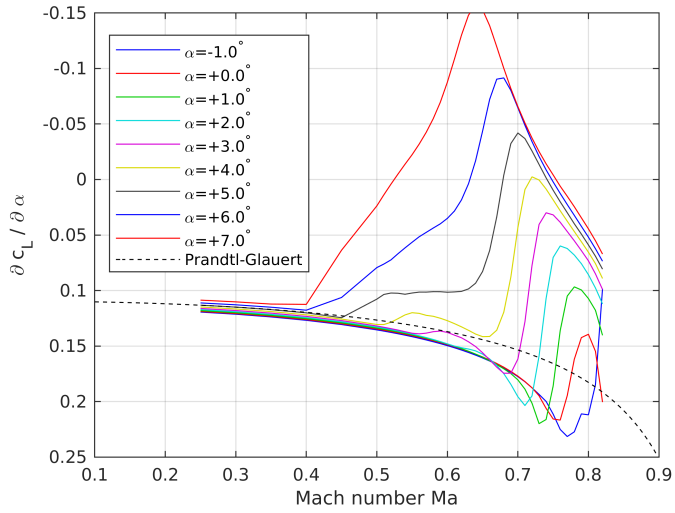

Figure 8: The quasi-steady lift polar slope $\partial c_L/\partial\alpha$ of the OAT15A airfoil as a function of Mach number and angle of attack.

these to the classic Prandtl-Glauert flat-plate value of $2\pi/\sqrt{1-Ma^2}$ (**Figure 8**). For low Mach numbers and AoAs the lift slope is nearly independent of angle of attack, indicating a potential-flow situation with negligible boundary layer effects. Around $Ma = 0.75$ a global maximum is visible (reversed ordinate) for low AoAs that clearly overshoots the theoretical flat-plate value. From this quasi-steady point of view it is reasonable to assume that also the unsteady aerodynamic response magnitude will become maximal at this point and the resulting flutter boundaries exhibit a minimum.

Before we use the 2-DOF heave-pitch OAT15A model for actual production runs in the transonic separated flow regime we aim at an initial verification of the three flutter prediction methods at moderate subsonic conditions ($Ma = 0.5$ and $\alpha = 0°$). We study the eigenvalues of the coupled system as a function of the stability parameter ρ in a classic bending-torsion flutter scenario. **Figure 9** shows the result of the eigenvalue approximations (made non-dimensional with c/V) during a density sweep for the three different methods (baseline structure). At $\rho \approx 0.48$ kg m^{-3} the torsion branch becomes unstable. A little later, at $\rho \approx 0.74$ kg m^{-3} a static divergence instability occurs. All three methods correctly predict the primary flutter branch and the zero crossing of the real part but behave rather differently in the entire complex plane. RFA and SCM agree well for the heave branch, where NPK starts deviating with increasing distance from the imaginary axis. The RFA is run here with a fixed polynomial order of 8, which appears to be over-fitting in this case. The resulting poles on the real axis move erratically and are likely non-physical. While RFA and SCM are globally approximating ("curve-fitting") methods, NPK can be viewed as exact but with the limitation that the "wrong" eigenvalue problem ("p-k" instead of "p-p") is solved and therefore can be regarded as physically exact on the imaginary axis only. Interestingly, NPK realizes the static-divergence zero crossing by a rather non-physical spontaneous birth of a pair of new conjugate poles. SCM predicts the most realistic scenario in which a real-valued *fluid eigenvalue* evolves towards static divergence. We will recognize these characteristics later in other flow situations.

We now employ the three eigenvalue methods (that can be expected to agree in the zero-damping case) to predict the flutter boundary at $\alpha = 0°$ over a broad range of Mach numbers. We compare three different stiffness configurations. **Figure 10** shows the stability boundaries in terms

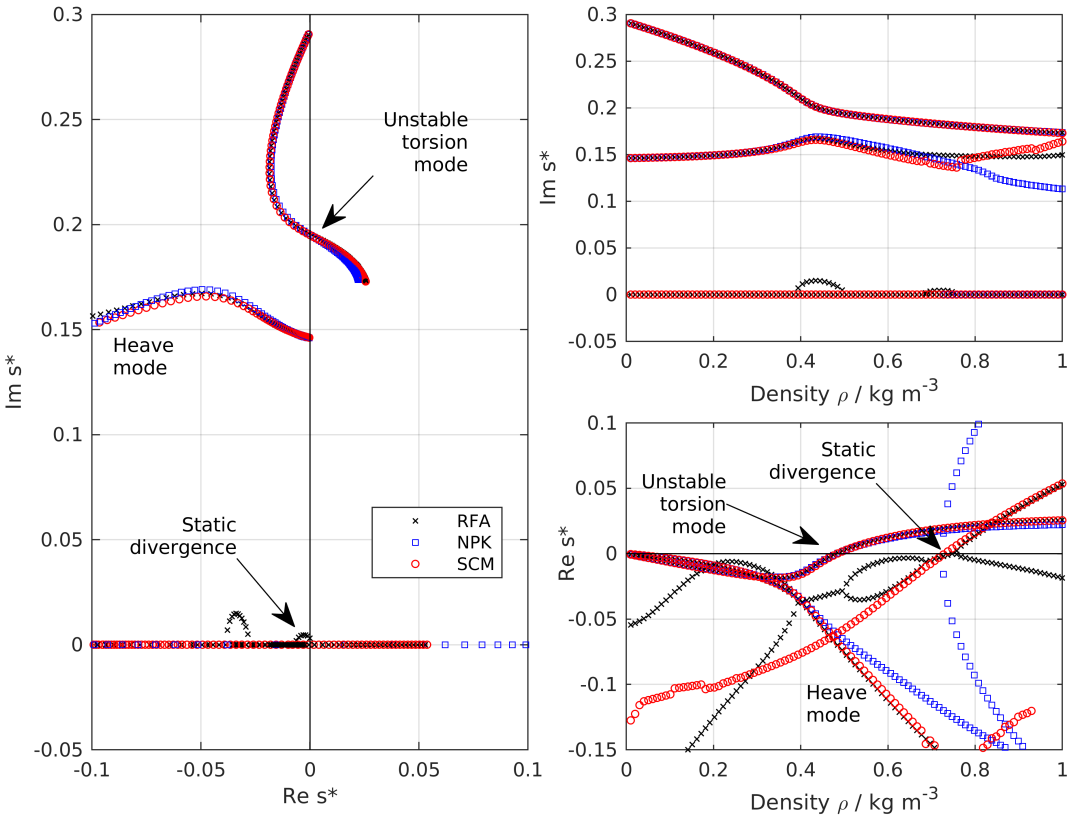

Figure 9: Complex coupled-system eigenvalues as a function of density ρ

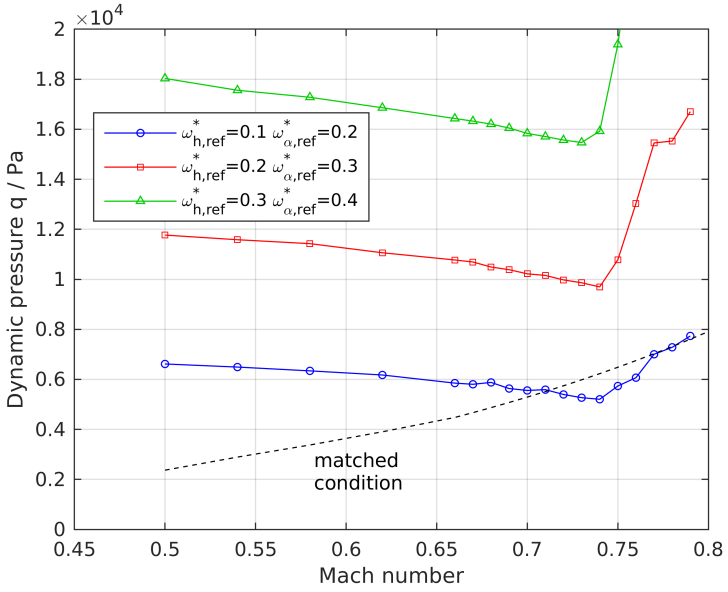

Figure 10: Flutter boundary at $\alpha = 0°$ for three different stiffness configurations

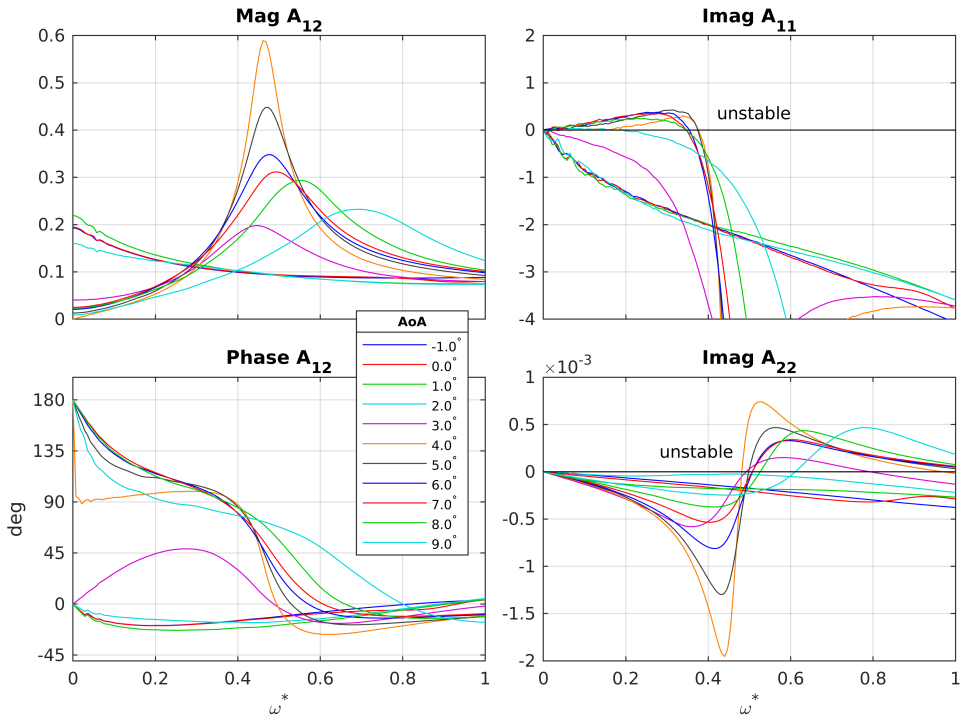

Figure 11: Aerodynamic FRF at Ma=0.73 depending on angle of attack

of the critical dynamic pressure $q = \rho V^2/2$ at $\alpha = 0°$. A typical Transonic Dip shape can be observed, independent of the structural eigenfrequency characteristics. The dashed line indicates the atmospheric conditions of the actual RANS simulations. The Transonic Dip minimum agrees well with the lift slope maximum in Figure 8.

Before we move on to study the effect of angle of attack and flow separation on the flutter behavior we analyze the unsteady aerodynamic response at $Ma = 0.73$. **Figure 11** shows the aerodynamic FRF for various angles of attack. At small incidence the FRF has a classic Theodorsen-like shape. With increasing AoA a clearly visible aerodynamic resonance peak protrudes with an amplitude maximum at $\omega^* \approx 0.45$. This value is in good agreement with the shock buffet frequency measured in the wind tunnel experiment [10]. Damping and peak frequency increase further with increasing AoA. Contrary to the wind tunnel experiment, all flows are fixed-point stable at $Ma = 0.73$ which may be attributed to turbulence modelling and grid effects. Nevertheless, we are apparently close to the self-excited shock buffet region at slightly lower Mach numbers (compare [12] for similar RANS simulations). Note that the imaginary part of the main diagonal GAF derivatives (the response of the lift to a heaving motion and the response of the aerodynamic moment to a pitching motion) become positive in a certain frequency range, indicating that pure one-degree-of-freedom flutter is possible individually for both heave and pitch.

We use the unsteady aerodynamic responses sampled at various angles of attack beforehand for detailed eigenvalue analyses to calculate the critical flutter stability limit as a function of α. **Figure 12** shows the resulting flutter boundaries for the three structural configurations already known from the Transonic Dip curves in Figure 10. It is apparent that the variation due to angle of attack is much larger than the variation due to Mach number. With increasing angle of attack the flutter boundary, initially, shows a rapid increase, followed by a rapid decrease and a local minimum at $\alpha = 4°$. The minimum value decreases with increasing structural

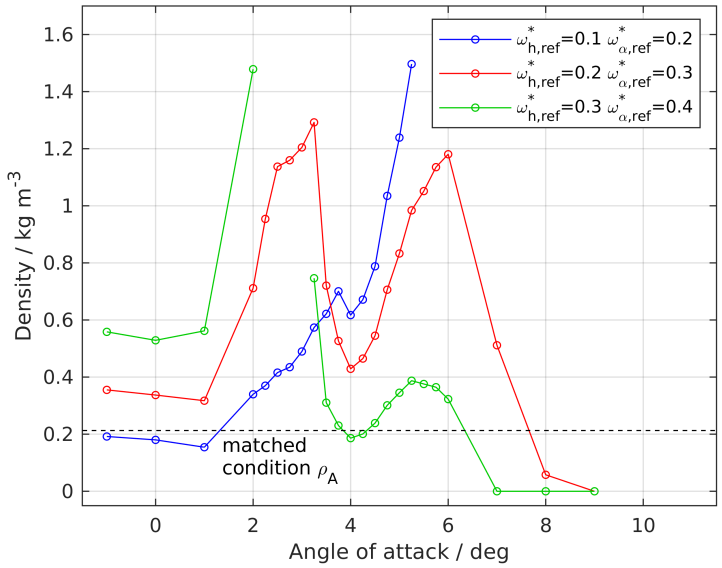

Figure 12: Flutter boundary as a function of angle of attack at at Ma=0.73 for three different stiffness configurations

stiffness (or increasing structural eigenfrequencies) and can clearly undercut the reference value at $\alpha = 0°$. The curves in Figure 12 comprise different flutter mechanisms that are analyzed in the following.

Figure 13 shows the coupled root loci of the medium-stiffness variant ($\omega^*_{h,ref} = 0.2$, $\omega^*_{h,ref} = 0.3$, red curve in Figure 12) at selected AoAs for virtual density sweeps from 0 to 1.5 kg m^{-3}. At $\alpha = 0°$ we observe the familiar bending-torsion flutter, this time with the heave branch getting unstable. The static divergence instability is already present at higher ρ values and takes over at $\alpha = 2.5°$. At this angle, SCM already identifies a completely new strongly damped fluid eigenvalue in the coupled response at $\omega^* \approx 0.35°$ while the torsion branch evolves into static divergence. At $\alpha = 3°$ RFA and SCM agree well on the mechanisms while NPK has developed an independent branch too. Static divergence still dominates. At $\alpha = 3.5°$ the fluid mode takes over. NPK realizes the zero crossing once more via spontaneous birth of a pair of poles that quickly separate in opposite directions. At $\alpha = 4°$ the aerodynamic response magnitude reaches a maximum (recall Figure 11) and hence the initial damping of the fluid mode reaches a minimum and gets even more amplified when coupling with the structural torsion DOF. At higher angles of attack the fluid mode gets more damped and increases in frequency. A second loss of the flutter stability occurs when the topology of the root loci changes suddenly and now the torsion branch becomes unstable as it gets dragged quickly into the 1-DOF torsion flutter frequency range above $\omega^* = 0.5$ (positive imaginary part of A_{22} in Figure 11).

To answer the question whether the fluid-mode flutter mechanism is essentially a coupling between the initially damped shock buffet fluid mode and the structural torsion mode *only* we repeat the previous flutter analysis at $\alpha = 3.5°$ with the heave DOF blocked (**Figure 14**). The results clearly confirm, that an active heave DOF is not necessary. We apply the same 1-DOF pitch-only setup to investigate the impact of the RANS turbulence modelling on the observed fluid-mode flutter phenomenon. In **Figure 15** we show the aerodynamic FRF at $\alpha = 3.5°$ (and at $\alpha = 0°$ for reference). The resulting root loci correlate very well with the aerodynamic FRF.

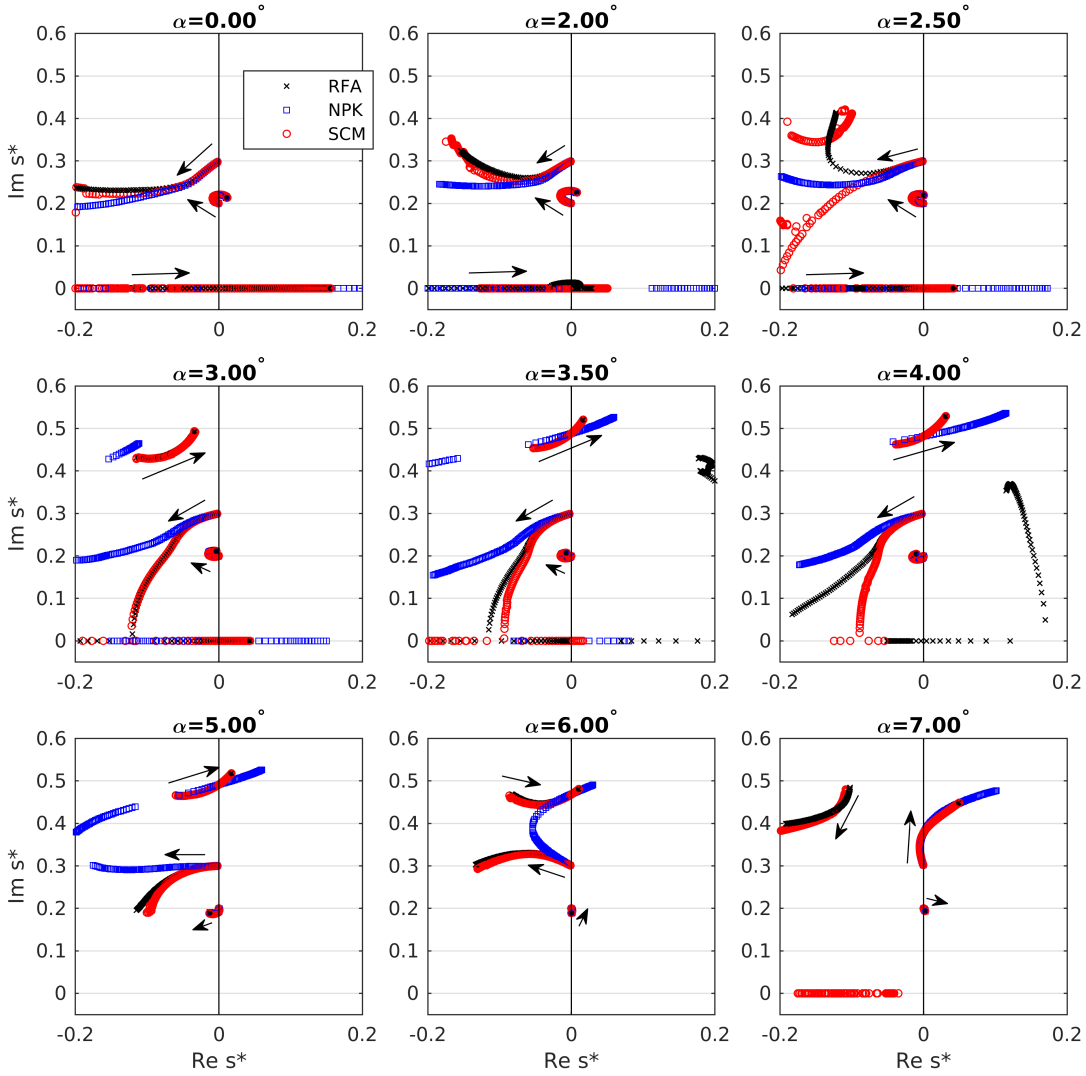

Figure 13: Evolution of the approximate coupled-system eigenvalues during the virtual density sweeps at selected angles of attack corresponding to Figure 12 ($\omega^*_{h,ref} = 0.2$, $\omega^*_{h,ref} = 0.3$).

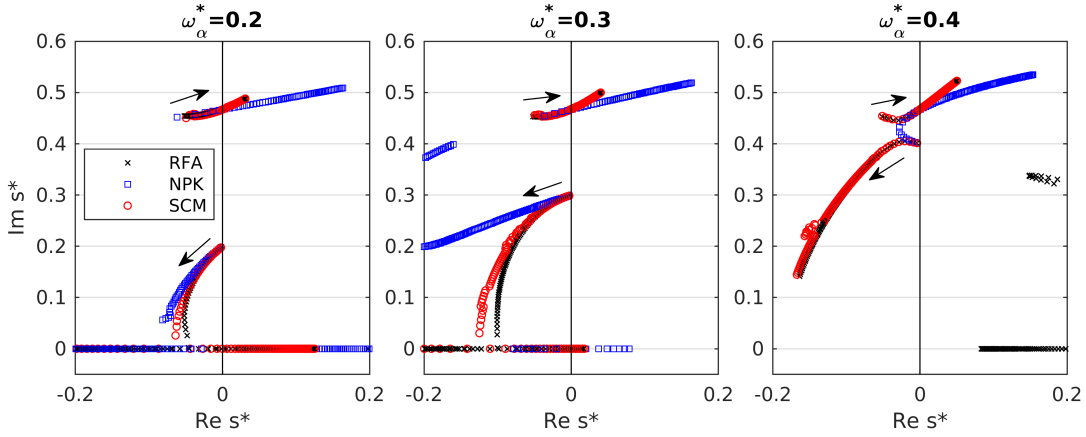

Figure 14: Evolution of the approximate coupled-system eigenvalues during the virtual density sweep from 0 to 1.5 kg m^{-3} at $\alpha = 3.5°$ with increasing torsional stiffness (heave DOF blocked).

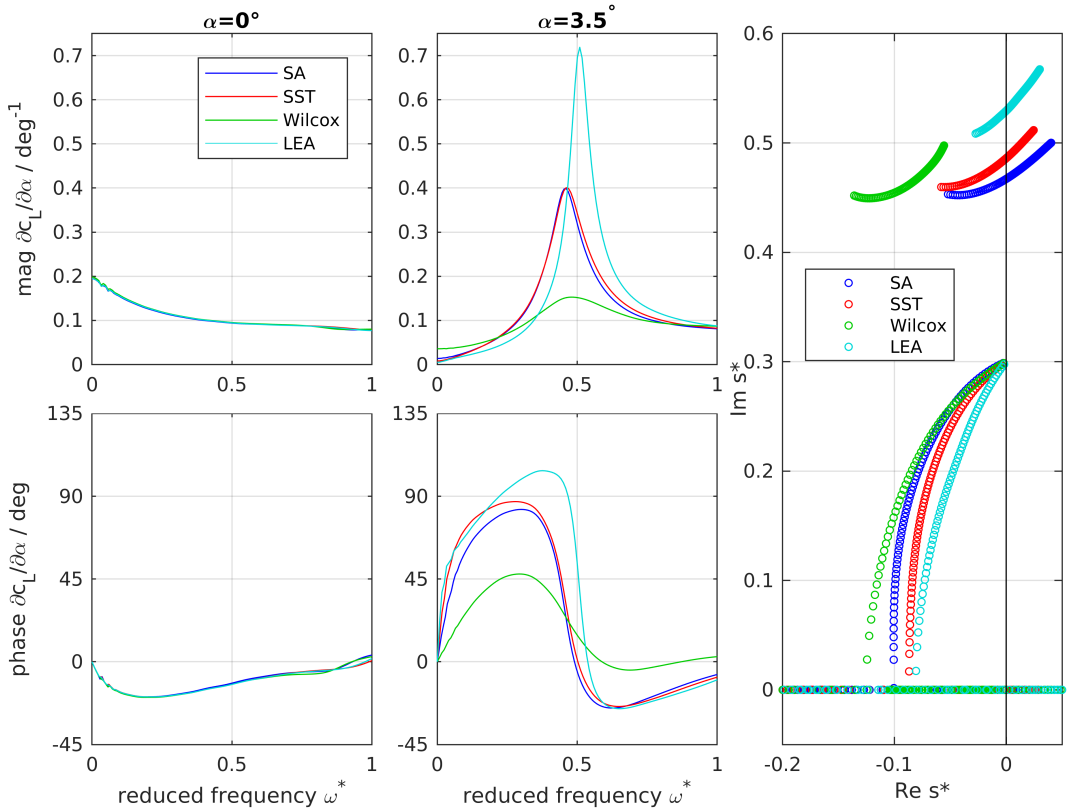

Figure 15: Effect of different RANS turbulence models on the aerodynamic FRF and the resulting fluid-mode flutter behavior (heave DOF blocked, RFA method only).

3.2 Symmetric flexible-plate airfoil

In the symmetric flexible-plate airfoil case the airfoil thickness t takes over the role of the angle of attack with the salient difference that, in the steady case, both sides experience exactly the same shock and boundary layer situation. With increasing thickness, similar to the OAT15A airfoil, regular shock motion is followed by inverse shock motion as shock-induced boundary layer separation sets in and a lambda shock system forms. The resulting re-circulation bubble extends over the aft part and reattachment may occur. The second geometric parameter we consider in this paper is the length L of the flat plate attached to the trailing edge. Since the curvature vanishes completely at $x = 1$ (start of the plate) no visible disturbance is introduced to the pressure distribution. Interestingly, increasing L from zero has nearly no effect at all on the *steady* pressure field in the front part.

Early *unsteady* RANS simulations indicate at least *two* types of qualitatively different transonic flow instabilities beyond critical values of Mach number and thickness. Notably, both of these instabilities are *anti-symmetric* in nature, i.e. when the upper-side shock moves downstream the lower-side shock moves upstream and vice versa. The instability regions partly overlap in the $Ma - t$ plane. In the stable-flow regime outside the two individual instability onsets a series of aerodynamic resonance peaks can be detected over a broad frequency range. **Figure 16** shows an exemplary aerodynamic FRF of the GAF derivative A_{11}, i.e. the generalized aerodynamic force corresponding to the first plate bending mode with respect to a deflection of this very bending mode and, hence, is the relevant quantity for the estimation of the possibility of one-degree-of-freedom flutter. The FRF is dominated by a resonance peak at $\omega^* \approx 2$ that corresponds to the mentioned second *high-frequency* instability. Another high-frequency resonance

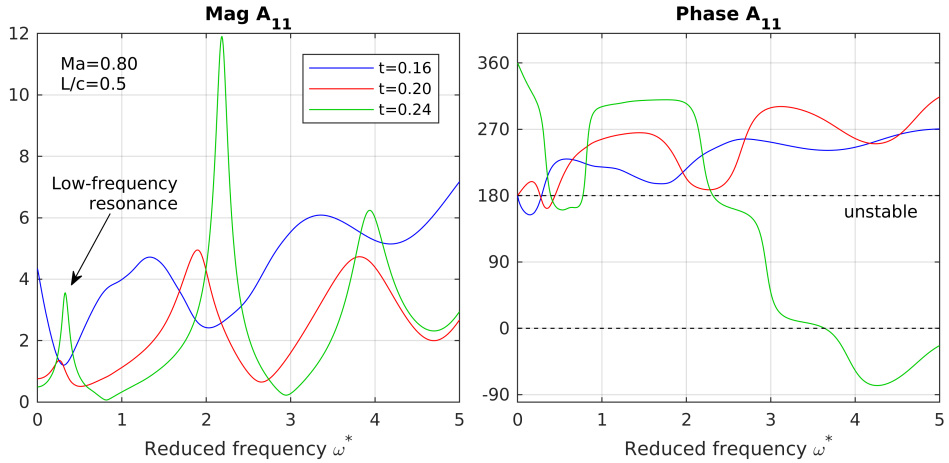

Figure 16: Influence of the airfoil thickness t on the aerodynamic FRF ($Ma = 0.8$, $L = 0.5$)

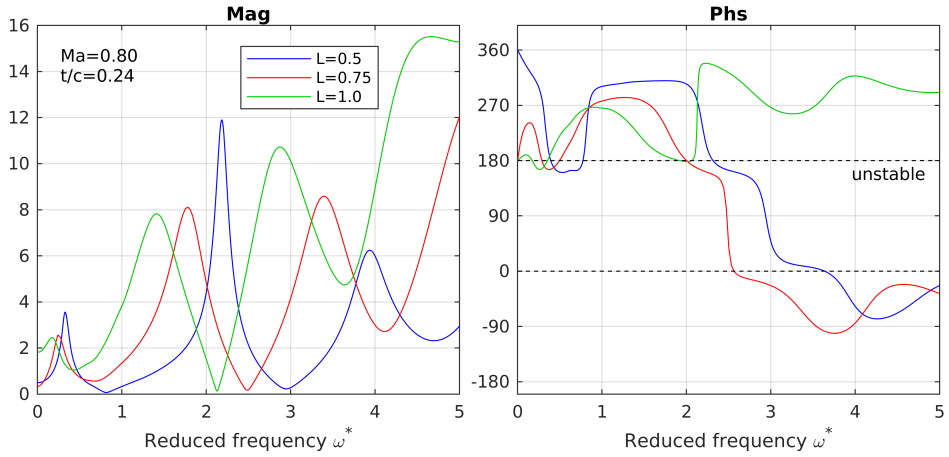

Figure 17: Influence of the plate length L on the aerodynamic FRF ($Ma = 0.8$, $t = 0.24$)

appears at roughly twice that value. Note that the simulation time step size of $\Delta t^* = 0.025$ is likely not sufficient to accurately resolve these high-frequency mechanisms. More important in the context of airfoil shock buffet is the *low-frequency* peak at $\omega^* \approx 0.35$ that forms with increasing t and corresponds to the first of the two mentioned flow instabilities. Visual inspection of the unsteady flow solutions indicate a high degree of similarity to the one-sided OAT15A airfoil buffet. The FRF characteristics are similar as well: At $t = 0.24$ a positive imaginary part (negative damping) occurs in a frequency range immediately above the resonance frequency. The phase value of $360°$ (or $0°$) at $\omega^* = 0$ means a positive sign of the real part and immediately points at the occurrence of static divergence.

While the plate length L has no significant effect on the steady airloads, it considerably changes the unsteady aerodynamic response. **Figure 17** shows the FRFs for different plate lengths at $Ma = 0.8$ and a thickness of $t = 0.24$. With increasing plate length, the resonances (and anti-resonances in between) shift to lower values, clearly indicating a positive correlation of the oscillation period with L, while the overall characteristics stay qualitatively intact. An increasing plate length also increases the damping of the low-frequency fluid mode and is observed to even stabilize an unstable flow.

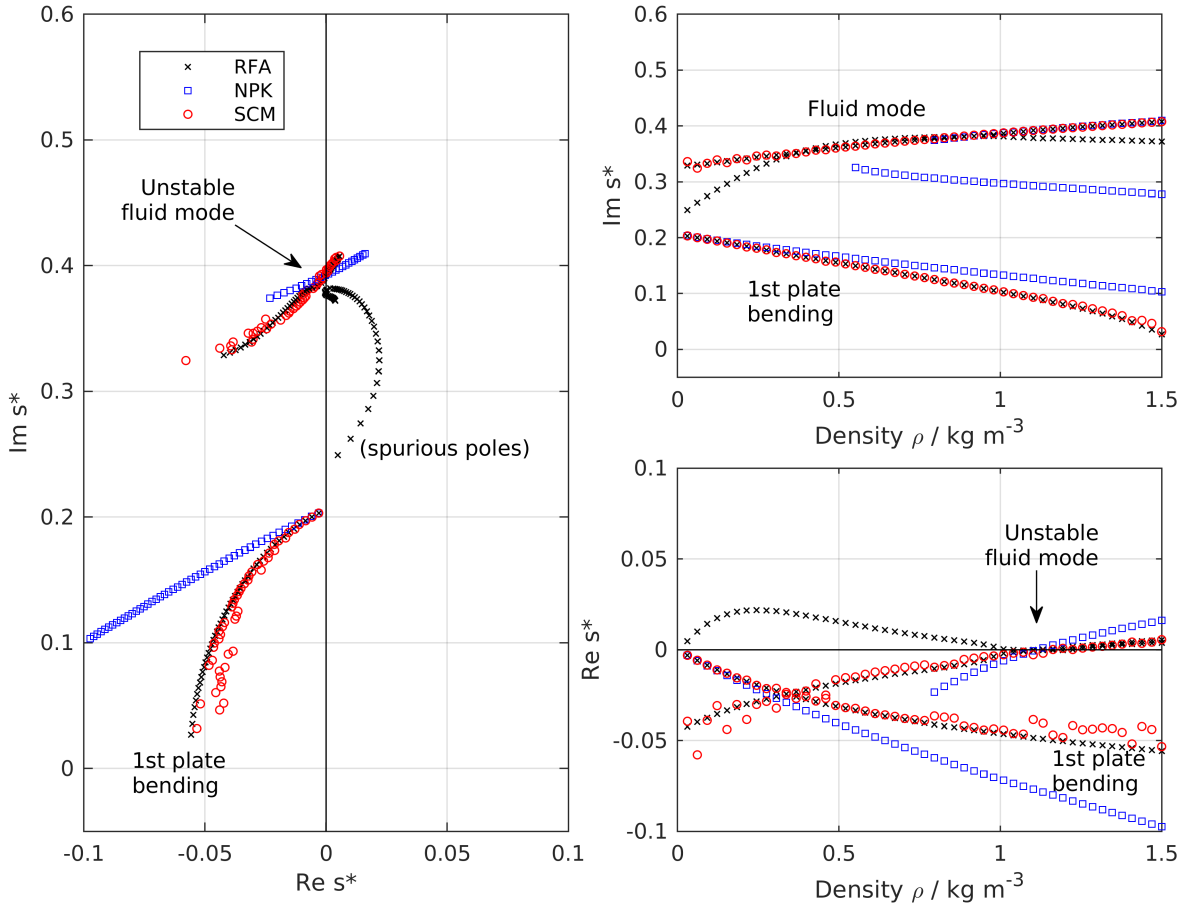

Figure 18: Flutter behavior of the symmetric flex-plate airfoil at $Ma = 0.8$ ($L = 0.5$, $t = 0.24$, 1-DOF only)

To test the symmetric airfoil configuration for the general possibility of fluid-mode flutter we investigate the stable-flow situation ($L = 0.5$, $t = 0.24$, $Ma = 0.8$) in combination with a flexible trailing-edge plate calibrated to a reduced vacuum eigenfrequency of $\omega_1^* \approx 0.2$ ($h = 2.6$ mm, material: steel) with only the first structural plate bending mode taken into account. **Figure 18** shows the corresponding eigenvalue evolution during the virtual air density sweep. All three eigenvalue methods clearly predict an unstable fluid mode branch at $\omega^* \approx 0.35$, matching with the low-frequency peak in Figures 16 and 17. The bending mode evolves towards static divergence. The general behavior is very similar to the single-degree-of-freedom OAT15A case (cf. Figure 14).

4 CONCLUSIONS

We have investigated the unsteady aerodynamics and the linearized flutter stability behavior of a 2-DOF heave-pitch OAT15A airfoil and a generic symmetric airfoil of variable thickness equipped with a flexible trailing-edge plate by means of 2-d RANS simulations. In both cases transonic pre-buffet flow situations involving shock-induced separation have been examined with regard to the occurrence of resonance peaks in the aerodynamic frequency response. These resonances correspond to fluid modes with complex eigenvalues. It has been shown that coupling the initially stable flow with an elastic structure can change the fluid eigenvalues and even destabilize an initially stable fluid mode due to mutual interaction.

It may appear to the observer of fluid mode flutter that the buffet onset gets magically reduced

to lower critical values in the presence of an elastic fluid boundary. The latter would make no sense when thinking in the classic categories of *buffet*, denoting the fluid instability within fixed non-moving boundaries, and *buffeting*, denoting the response of an elastic structure to the loads induced by that instability. It makes perfect sense, when we interpret buffeting essentially as an instability of a fluid-structure coupled system (flutter) and the buffet onset as the limiting case of that flutter boundary at zero density or infinite mass ratio.

The flutter analysis method to find the coupled eigenvalues plays a crucial role in the analysis of the phenomenon. The p-k assumption has been shown to have some limitations in the accurate recovery of the fluid mode root loci. The negative effect could be worsened when the root search is limited to tracking the structural poles only, starting from the vacuum eigenfrequencies. Globally approximating pole-fitting methods like rational function approximation or the time-domain successive convolution in combination with an identification method like ITD/DMD as discussed in this paper are promising candidates for future improvements.

ACKNOWLEDGEMENTS

The research leading to this work has received funding from the European Union's Horizon 2020 research and innovation program under grant agreement number 769237 (project HOMER).

5 REFERENCES

[1] Abbas-Bayoumi, A. and Becker, K. (2011). An industrial view on numerical simulation for aircraft aerodynamic design. *Journal of Mathematics in Industry*, 1(1), 10. doi: 10.1186/2190-5983-1-10.

[2] Nitzsche, J. (2009). A numerical study on aerodynamic resonance in transonic separated flow. In *Proc. of the 14th International Forum on Aeroelasticity and Structural Dynamics (IFASD), Seattle, WA, USA, 22-24 June 2009*.

[3] Iovnovich, M. and Raveh, D. E. (2011). Transonic unsteady aerodynamics in the vicinity of shock-buffet instability. In *Proc. of the 15th International Forum on Aeroelasticity and Structural Dynamics (IFASD), Paris, France, 27-30 June 2011*.

[4] Giannelis, N. F., Vio, G. A., and Levinski, O. (2017). A review of recent developments in the understanding of transonic shock buffet. *Progress in Aerospace Sciences*, 92, 39–84. doi:10.1016/j.paerosci.2017.05.004.

[5] Crouch, J. D., Garbaruk, A., Magidov, D., et al. (2009). Origin of transonic buffet on aerofoils. *Journal of Fluid Mechanics*, 628, 357–369. doi:10.1017/S0022112009006673.

[6] Iorio, M. C., González, L. M., and Ferrer, E. (2014). Direct and adjoint global stability analysis of turbulent transonic flows over a NACA0012 profile. *International Journal for Numerical Methods in Fluids*, 76, 147–168. doi:10.1002/fld.3929.

[7] Crouch, J. D., Garbaruk, A., and Strelets, M. (2018). *Global Instability Analysis of Unswept- and Swept-Wing Transonic Buffet Onset*. doi:10.2514/6.2018-3229.

[8] Timme, S. *Global Shock Buffet Instability on NASA Common Research Model*. doi: 10.2514/6.2019-0037.

[9] Deck, S. (2005). Numerical simulation of transonic buffet over a supercritical airfoil. *AIAA Journal*, 43, 1556–1566. doi:10.2514/1.9885.

[10] Jacquin, L., Molton, P., Deck, S., et al. (2009). Experimental study of shock oscillation over a transonic supercritical profile. *AIAA Journal*, 47, 1985–1994. doi:10.2514/1.30190.

[11] Illi, S., Lutz, T., and Krämer, E. (2012). On the capability of unsteady RANS to predict transonic buffet. In *Third Symposium "Simulation of Wing and Nacelle Stall", Braunschweig, Germany, 21-22 June*.

[12] Giannelis, N. F., Levinski, O., and Vio, G. A. (2018). Influence of Mach number and angle of attack on the two-dimensional transonic buffet phenomenon. *Aerospace Science and Technology*, 78, 89 – 101. doi:10.1016/j.ast.2018.03.045.

[13] Zimmermann, D.-M., Mayer, R., Lutz, T., et al. (2018). Impact of Model Parameters of SALSA Turbulence Model on Transonic Buffet Prediction. *AIAA Journal*, 56, 874–877. doi:10.2514/1.J056193.

[14] Gustavsen, B. and Semlyen, A. (1999). Rational approximation of frequency domain responses by vector fitting. *IEEE Transactions on Power Delivery*, 14(3), 1052–1061. doi:10.1109/61.772353.

[15] Ibrahim, S. and Mikulcik, E. (1977). A method for the direct identification of vibration parameter from the free response. *Shock and Vibration Bulletin*, 47, 183–198.

[16] Poplingher, L., Raveh, D. E., and Dowell, E. H. (2019). Modal analysis of transonic shock buffet on 2d airfoil. *AIAA Journal*. doi:10.2514/1.J057893.

COPYRIGHT STATEMENT